Internal waves and bottom currents interactions around mesophotic reefs, southeastern Mediterranean

Or M. Bialik[1,2,3*]; Omri Gadol[4]; Aaron Micallef[3]; Christian Betzler[5]; Hagai Nativ[6]; ; Yizhaq Makovsky[1,4]

1. Dr. Moses Strauss Department of Marine Geosciences, The Leon H. Charney School of Marine Sciences, University of Haifa, Carmel 31905, Israel.

2. Institute of Geology and Palaeontology, University of Münster, Corrensstr. 24, 48149 Münster, Germany

3. Marine Geology & Seafloor Surveying, Department of Geosciences, University of Malta, Msida, MSD 2080, Malta.

4. Hatter Department of Marine Technologies, Charney School of Marine Sciences, University of Haifa, Mount Carmel, 31905 Haifa, Israel.

5. Institute of Geology, CEN, University of Hamburg, Bundesstrasse 55, Hamburg 20146, Germany.

6. Morris Kahn Marine Research Station, The Leon H. Charney School of Marine Sciences, University of Haifa, Haifa, Israel

*Corresponding author (obialik@uni-muenster.de, obialik@campus.haifa.ac.il)

Submitted for review in *Sedimentology*

ABSTRACT

Mesophotic reefs are found in water depths greater than 30m and as such are, for the most part, removed from most direct wave activity, notably in the Mediterranean Sea. There, they are protected from anthropogenic impact and serve as a possible refuge for marine biodiversity in a warming ocean. Yet, like any reef, their growth is modulated by the distribution of the sediment they produce and supply of nutrients. Here we explore the mechanisms governing the sediment distribution around a coralligenous mesophotic reef system as a case study of the long-term governing mechanisms in this environment. A detailed survey of a mesophotic reef offshore Israel was carried out using acoustic imaging from an autonomous underwater vehicle. This survey generated a highly detailed (cm-scale) resolution dataset with wide area coverage of the sediment distribution patterns around the reef. The mesophotic reefs are built as a series of asymmetric ridges with biogenic sediment filling the depressions between them. Two types of sediment bedforms were identified in the sediment fill - elongated linear bedforms aligned north-south; and intersecting smaller bedforms aligned NW-SE and NE-SW, forming chevron-like shapes. Both types of bedforms are composed of coarse-grained material (sand to gravel) and their distribution is partially related to their location relative to the hard substrate. The bedform present and the ridge asymmetry points to a prominent role of a south-to-north bottom current. These current supplies nutrients to the reefs, but also loads sediment on their southern side, leading to asymmetry. Additionally, the chevron bedforms are attributed to interactions with the rocky substrate and internal waves. These internal waves likely also play a role in modulating the reefs' growth. The geometries and growth of mesophotic reefs, and the distribution of the sediment around them, are controlled by the combination of both internal waves and bottom currents.

Keywords: Levant, Sediment distribution, Contourites, Synthetic Aperture Sonar, Coralline Algae

INTRODUCTION

Benthic communities, notably reefal, in depths between ca. 30m and 150m, are commonly referred to as "mesophotic" (Baker et al., 2016). Due to this depth being too shallow for oceangoing large research vessel but too deep for recreational divers, it is largely understudied. This is despite the potential importance of the reefal communities in this zone. Notably, as a refugia from various environmental disturbances, such as climate change and anthropogenic disturbances (Bongaerts et al., 2010; Martinez et al., 2021). The exact definition of this zone is not universally agreed, with many overlapping definitions and the use of other terms such as "the twilight zone" or "mid photic zone" in different publications (Bradford and Chang, 1987; Brokovich et al., 2008; Mitchell et al., 2000). This is a general term that encapsulates the range where light availability is reduced past its inflection point (~20%) and declines at a slower rate. The oceanographic conditions these reefs are exposed to, often being located below or on the pycnocline, are significantly cooler and more nutrient enrich compared to shallower reefs (Kahng et al., 2019; Richardson & Bendtsen, 2019). Mesophotic reefs exhibit a different benthic community and composition than reefs in shallower waters (Kahng et al., 2014; Rocha et al., 2018), and can have a significant coralline algae constituent (Amado-Filho et al., 2016). This coralline component means that the sediment and framework (coralligenous) production in mesophotic carbonate factories should be more similar to that of a C-Type factory (*sensu* Schlager, 2005), with significant local grain export. The depth in which mesophotic reefs are located means that the processes that distribute sediments in shallower water reefs, such as waves and tides, are not able to generate the same effects these deeper environments. Because of constraints with working in mesophotic depths, the processes governing and shaping mesophotic environments are poorly described and constrained (Smith et al., 2016).

Following the initial experimental work of Cacchione (1970), it has been suggested that internal waves may play a significant role in modulating turbidity, nutrients, heat and sediment distribution in mesophotic settings (Cacchione and Drake, 1986; Kahru, 1983; Pomar et al., 2012; Wolanski and Delesalle, 1995) as well as influence the evolution of reefs (Leichter et al., 1998; Lesser et al., 2009; Pomar et al., 2017; Schmidt et al., 2016; Wang et al., 2007; Wyatt et al., 2020). Internal waves are oscillations that propagate along internal stratification boundaries in the ocean (Talley et al., 2011). These waves are mostly generated by tides, but can be induced by wind waves as well (Nagasawa et al., 2000; Polton et al., 2008). Similar to waves at the ocean surface, internal waves also break, transferring energy and changing frequency as they approach the seafloor. These internal wave breaks are an important dissipation and mixing mechanism, as they can disrupt the pycnocline (Lamb, 2014). If encountering an elevated structure,

such as a reef, internal waves may also shallow and break (Davis and Monismith, 2011). The interaction of internal waves of different frequencies with the seafloor can resuspend and redistribute sediment in a similar fashion to wind waves nearshore (Boegman and Ivey, 2009; Cheriton et al., 2014; Quaresma et al., 2007). In addition to turbulence, the breaking of internal waves can redistribute heat and nutrients, inflicting a significant impact on deeper shelf / upper slope benthic communities (Woodson, 2018). However, the way these waves interact with the seafloor in the mesophotic environment is poorly understood, as is the nature and type of bedforms they form (van Haren, 2017).

Another modulator of seafloor state in mesophotic environments is bottom currents, which range from slope parallel to slope perpendicular (Church et al., 1985; Silva and MacDonald, 2017; Valle-Levinson et al., 2020; Williams et al., 1984). These currents both shape the sediment distribution around the reefs and may have a role in recruitment and larva distribution. The effects of such currents on lateral connectivity are not entirely clear, as the genetic relations between communities along mesophotic belts exhibit variable patterns (Bongaerts et al., 2013; Studivan and Voss, 2018). This is possibly due also to issues related to light modulation (Laverick et al., 2020). The interaction with these bottom currents, be them slope vertical or lateral, can also modulate the nutrient and temperature state to a level that may result in population shifts between periods of different current regimes (James et al., 1999; James and Lukasik, 2010).

Understanding the nature of the seafloor interaction with both bottom currents and internal waves in the mesophotic setting is essential to better protect and manage these environments, as well as for core understanding of their dynamics. The aim of this study is to examine, using new high resolution under water imagining technologies, what role do these two mechanisms play in mesophotic reefs. Here we use multiple data sets from offshore northern Israel (southeastern Mediterranean), including high resolution Autonomous Underwater Vehicle (AUV) survey, Chirp sub bottom profiler, diving photography and sediment sampling, as well and physical oceanography data. Combined, these are used to constrain the governing long-term mechanism of sediments distribution around a series of mesophotic reefs, as recorded by the sedimentary system, their significance and potential impacts on the mesophotic community.

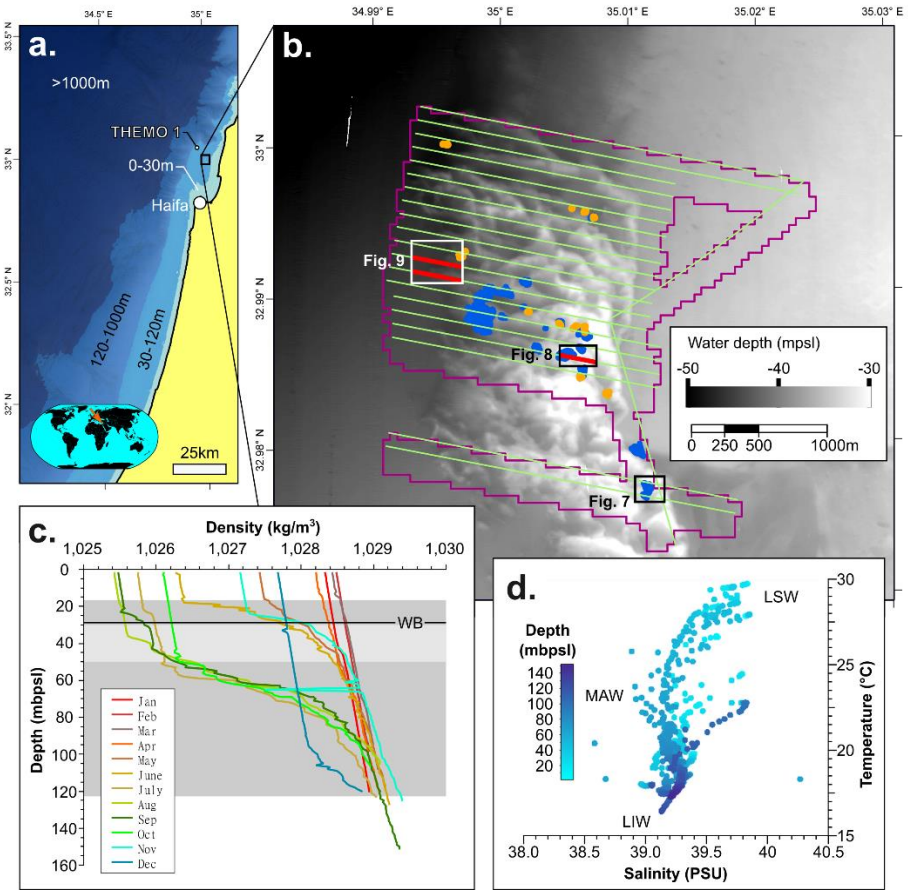

Figure 1: a. Map of Israeli and southern Lebanese shelf showing the position of the study area and location of the THEMO 1 buoy, inset shows the location of this map relative to the globe. b. Map of the study area, showing the overall bathymetry and location of Bustan HaGalil ridge, areas of manual mapping of sediment bedforms and rocks (blue and orange, respectively) as well as location of seismic lines (green), purple polygon delineates the outer parameter of the AUV survey. c. Annual variation in temperature at THEMO 1 in the top 150m (data from Reich et al., 2021), dark grey band outlines the annual amplitude of the pycnocline, light grey the depth distribution of sediment bedforms observed in this study, black line denotes the 99 percentile of effective wave depth which we consider as our wave base (WB). d. salinity/temperature for the too 150m at THEMO 1. MAW – modified Atlantic waters, LSW – Levant surface waters, LIW – Levant intermediate waters.

GEOLOGICAL SETTING

Sediment distribution along the southeastern margin of the Levant Basin (Figure 1a) is controlled by coast-parallel current and jets, swept towards the coast in shallower water by wave action (Almagor et al., 2000; Schattner et al., 2015). The continental shelf is 10 to 20 km wide, generally narrowing from south to north. This results with a significant decrease of the seafloor sediment grain size across the 30m isobath, from fine sand to very fine sand with a significant clay and silt fraction (Almogi-Labin et al., 2012). However, in the northern part of the Israeli shelf (north of ca. 32.6°N), at the edge of the Nilotic littoral cell (the main source of siliciclastic grains in the region), the coarser grain fraction increases and extends past the 40m

isobath. This region is characterized by a higher carbonate content (up to 47%; Almogi-Labin et al., 2012)), attesting for a higher relative contribution of local sediments supply. Sets of generally shore parallel aeolianite ridges (locally referred to as Kurkar Ridges) stretch along the coastal zone and the middle shelf (~30 to 40 m water depth) of Israel (Almagor et al., 2000). These underlying aeolianite ridges have developed repeatedly in the near shore, as controlled by the changing sea level during different Plistocene glacial cycles (Mauz et al., 2013; Shtienberg et al., 2017). The offshore ridges form one of the main hard substrates on the shelf and serve as the base of most offshore reefs in the region (Rilov et al., 2018). The internal structure and construction of these offshore reefs is poorly constrained as they are presently being overwhelmed by invasive species (Peleg et al., 2020; Rilov, 2013). They appear to be a composite construction of red and brown calcareous algae, bivalve and bryozoans. If similar to their presently coastal equivalents, the underlaying aeolianites are composed of a mixture of biogenic grains (molluscan aragonite and coralline algae high Mg calcite) and lithogenic quartz. These aeolianites are usually bounded by two generations of cement - an early grain coating micritic cement and a later pore filling sparry cement (Porat et al., 2003).

Some of the most prominent aeolianite ridges are found in the shelf of northern Israel, including our principal study area of the Bustan HaGalil Ridge (Eytam & Ben-Avraham, 1992; Sade et al., 2006; Figure 1a, b). This is an elongate, up to 10 m tall, complex system of seafloor ridges. It extends for 7 km in the north-south direction and up to ~1.5 km in the east-west direction between water depths of 27 to 50 m. the Bustan HaGalil Ridge acts as a boundary between the soft (mostly silty) seafloor sediments to the west of it and mostly hard carbonaceous seafloor to the east. Schattner et al. (2010) argued that has been forming a barrier for sediments infill, confining a low-energy depositional environment to the east of it since the early Holocene.

The Levant Basin hosts several main water masses that show seasonal depth variability (Alhammoud et al., 2005; Sisma-Ventura et al., 2016). During summer, the upper portion of the water column is comprised of two water masses, the warm and saline Levant Surface Water (LSW) between water depths of 0 and ca. 60 m, and the cooler and less saline Modified Atlantic Water (MAW) between water depths of 10 – 150 m. During winter, these two layers become mixed (Figure 1c, d). These water masses are underlain by the Levantine Intermediate Water (LIW) at depths of ca. 150 – 350 m, which oscillates on interannual scale (Ozer et al., 2017). The interfaces between these water masses facilitate the propagation of internal waves, which interact with the seafloor in the mid-to-outer-shelf and across the slope (Reiche et al., 2018). The nutricline in the Levant Basin does not overlap with the thermocline, notably in respect to nitrite and

phosphate (Kress and Herut, 2001; Krom et al., 2005). As a result, the basin is oligotrophic to ultra-oligotrophic year-long. Ongoing warming at unprecedented rates (Ozer et al., 2017; Rilov, 2016; Sisma-Ventura et al., 2014) further increases the ecological stress in the upper water column. These coincide in the coastal area with ongoing processes of species shift and "topicalization" of the Eastern Mediterranean with increasing temperatures (Bianchi, Carlo and Morri, 2003; Grossowicz et al., 2020; Rilov and Galil, 2009), which may change the production dynamics on these features in the future.

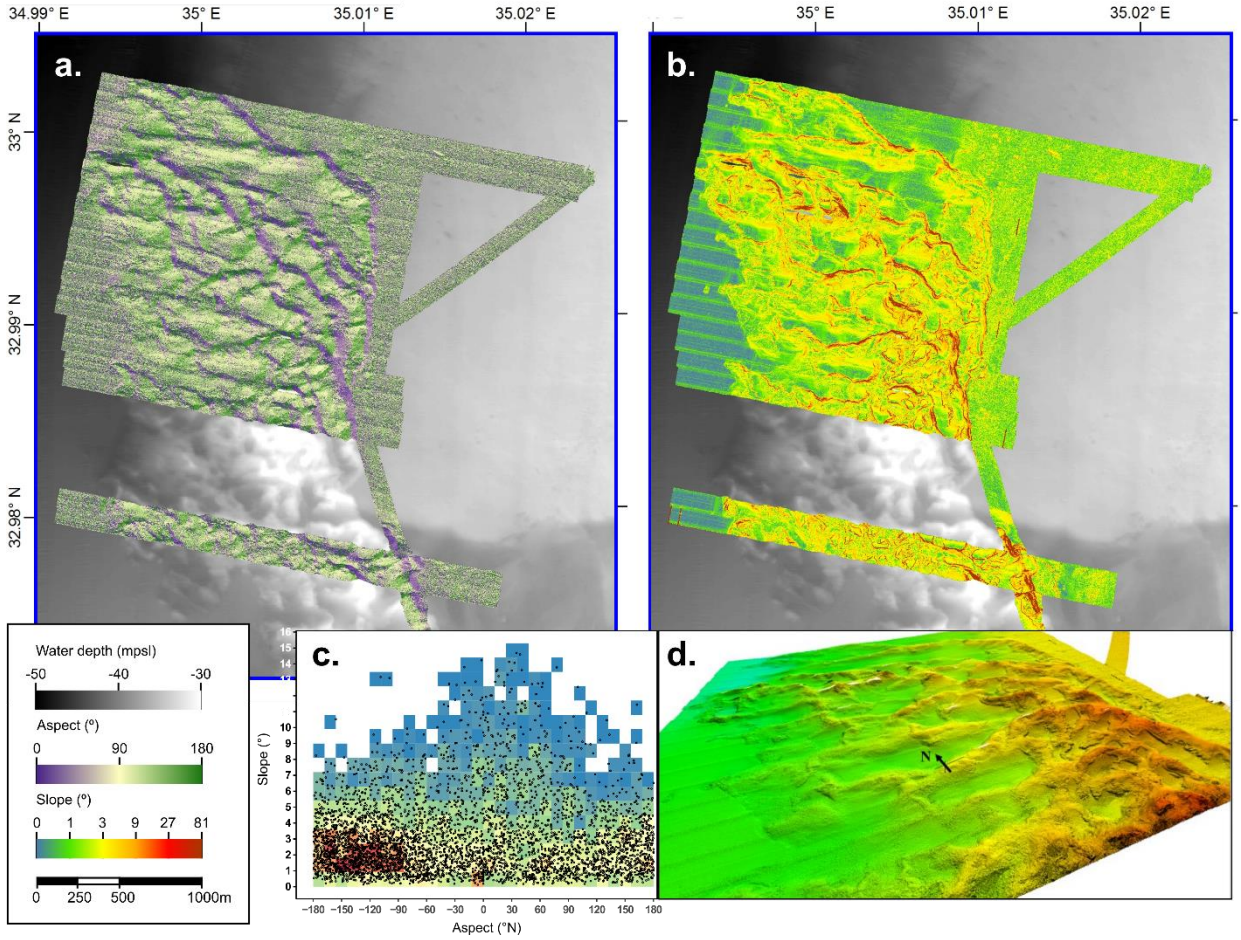

Figure 2: Bathymetric properties of the surveyed area: a. aspect; b. slope; c. density plot of the relations between aspect and slope, higher slopes occur with a NNW aspect while lower slopes are more concentrated in with a southern aspect; d. 3D shaded relief views of the Bustan Hagalil Ridge from a southeastern perspective, demonstrating the asymmetric nature of the features.

MATERIALS AND METHODS

A ultra-high-resolution geophysical investigation of the seafloor environment of Bustan HaGalil Ridge (Figures 1b, 2) utilized University of Haifa's ECA Robotics Inc. A18-UH deep-water surveying autonomous underwater vehicle (AUV) SNAPIR, operated off the Israel Oceanographic and Limnological Research

institute R/V Bat-Galim. The AUV survey was carried on May 22, 2019, acquiring a total of 47 km over the northern half of Bustan HaGalil ridge, at a flight elevation of 20 to 25 m above the seafloor in water depths of 25 to 50 m. Surveying included data acquisition with: (1) a Kraken Robotics MINSAS120 Interferometric Synthetic Aperture sonar (SAS), providing two-sided 100-m wide acoustic backscatter image swaths of the seafloor at 3-cm resolution; (2) a Norbit WBMS 400 kHz multibeam echo sounder, providing a 40 cm resolution bathymetric grid; (3) an Edgetech 2205 single channel sub-bottom profiler (SBP) using a 2 to 10 KHz Chirp signal, with a vertical resolution of ~20 cm. The SBP data were extracted as full-wave (Real) and processed and interpreted using AspenTech SSE software suite. Following real time application of the matching filter, post-processing scheme a minimum entropy deconvolution, 7.5 kHz high-cut filter and amplitude scaling. The multibeam bathymetry and SAS imagery were analyzed to identify the changes in seafloor character across the study area. Across three selected soft sediment rich areas of interest, in the west, central and east of the ridge, individual bedforms were manually traced and measured in ESRI ArcGIS. Both starboard and port side imaging were compared (Supplumnet 1, Figure S1-1) to verify no bias from illumination direction. In total, the crest lengths and directions of 8324 bedforms , and the widths of 5143 bedforms, were measured; values are given in the Supplementary Material (Table S1). Visualization of statistical analysis was carried out with a combination of ArcGIS, R software (R Core Team, 2020) with ggplot2 (Wickham, 2009) and QTIplot (Vasilief, 2010). Sizes and areas of some 1053 rock elements (small biogenic build-ups, see discussion below) were also measured. Sediment samples were collected via technical dives carried out at selected locations, which also visually documented the seafloor feature (Supplumnet 1, Figure S1-2). These sediment samples were washed with fresh water and air dried prior to microscopy analysis. Mineralogical analysis was carried out using a Rigaku MiniFlex XRD diffractometer. Grain size was evaluated both on the collected samples and by image analysis using ImageJ of quadrats (25cm x 25cm) collected during the dive.

Wave data were obtained from the long term THEMO1 buoy, located ~10 km from the study area, and available from the THEMO project's website (http://themo.haifa.ac.il/) (Figure 1a). Details of the processing of the wave data (following Allen, 1985; Clifton and Dingler, 1984) and data are given in the Supplementary Material (Supplement 2: Estimation of effective wave depth, Table S2). Brunt–Väisälä frequency was calculated based on density data (Figure 1c) collected monthly in 2018 and 2019 next to the THEMO 1 buoy in cruises described by Reich et al. (2021) and available through ISRAMAR (https://isramar.ocean.org.il/); values are included in cycles/hour and 10^{-2} rad 10^{-1} in Supplementary Material (Table S3). Subsequent data processing and visualization were done in R Software. All supplementary material is available via Figshare as 10.6084/m9.figshare.19642449.

RESULTS

Seafloor Types of the Bustan HaGalil Region

Based on the analysis of the available multibeam and SAS imagery, the Bustan HaGalil Ridge is composed of multiple crisscrossing north-south oriented and east-west oriented ridges (Figures 1b, 2; see also Supplement 1, Figure S1-3). The slopes in the study area range from 0° to 86° with the mean slope in the study area being 2.95°±3.12° (n=101,252,744). However, the ridges are asymmetric, with a wider southwest facing slope and an narrower northeast facies slope (Figure 2a). The north facing and east facies slopes are generally steeper (Figure 2b). Maximum slope angels reach 15° and are located on an arc between -30° from north and +60° from north (Figure 2c). The north-south component is more prominent and forms a backbone set of ridges along the eastern side of the Bustan HaGalil Ridge, from which the east-west components diverge westwards. Generally, elongated (~1km scale) and east-west trending valleys separate between the diverging ridges (Figure 2d). The seafloor in the Bustan HaGalil Ridge region is composed of three main substrate forms (Figure 3): reef/bioconstructions (reefs, rhodoliths, nodules etc.), ripple like bedforms and near flat sediment. The shelf sediment west of the ridge had been previously described to be silt to silty clay grained deposits (Almogi-Labin et al., 2012) and as such we infer this is the character of the near-flat sediment. In between the ridges are small (100-500m along an E-W trend, 50-10mm along an N-S trend) valleys with a flat floor (0° to 1°) where the ridges are ~100-250m in width. The floor of the valleys is not horizontal and the type, size and direction of bedforms may change spatially within them. The valleys floor's upper depth is ~35mbpsl in the east going to ~45mbpsl in the west, conforming approximately to the shelf slope outside the ridge. The ridges meet the sediment covered seafloor at a water depth of ~35 metres below present sea level (mbpsl) in the east and extend to a minimum depth of 25 mbpsl. The Bustan HaGalil ridge in its entirety has a dip to the west and meets the sediment covered seafloor at a water depth of 45 mbpsl, deepening northwards to 50 mbpsl.

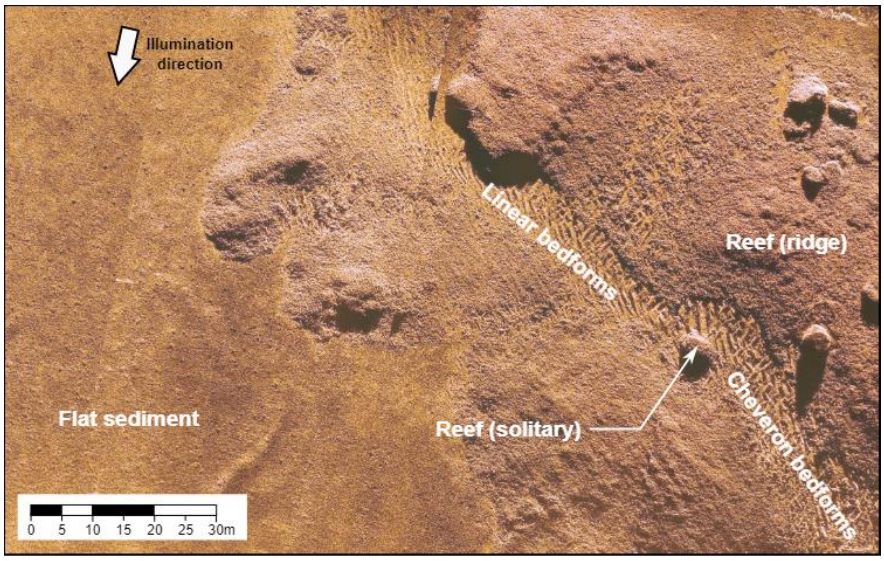

Figure 3: Wide scope mosaic of the SAS imaging in the western margin of the survey area showing the three main seafloor types in the study area.

Some small bedforms can be observed in this seafloor type but they are not as regular or clearly distinguished as the ripple-like bedforms occurring elsewhere in the study area. Most of the smaller bedforms are only visible with the SAS and cannot be distinguished with the multibeam (see Supplement 1, Figure S1-4), as such their relief is unknown. The rocks/bioconstructions occur either as solitary elements or large ridges/reefs, both with extensive biological coverage (see further description in subchapter 4.2. Sedimentary Description). We define any continuous rocky element larger than 10 m on its long axis with a defined relief as a ridge/reef. Similarly, we define any continuous solid mass smaller than 10 m on its longer axis, or on that scale but spatially separated than any other rocky mass, as a solitary reef/bioconstruction. This delineation was based on the observed sizes of the non-continuous rock masses. The solitary reefs/bioconstructions occur in two main forms - adjacent to a ridge (Figure 3, 4a) or scattered between bedforms regardless of any ridge (Figure 4b, 4c). The former was often observed to be larger than the latter. The solitary reef/bioconstruction vary in size from coarse gravel to boulders (on the Wentworth, 1922 scale) and are observed to occur in the trough between bedforms or at the end point of bedforms. Smaller (cm-scale) rocks/bioconstructions are often found in troughs, whereas larger rocks/bioconstructions are located at the end points of bedforms. Adjacent to boulder size rock/bioconstruction, a change in bedform character or direction is sometimes observed. The majority of rocky elements detectable in the seafloor images range from 0.13m to 20m along their long axis; the size distribution is highly skewed ($\tilde{\mu}_3$=5.2, n=1053; Figure 5) and over half the rocky elements are under 0.76m in length. This distribution marks around half of the rocky elements larger the what could be classified as rhodoliths, and as such immobile (Hottinger, 1983). The larger rock/bioconstruction and ridges/reefs

exhibit a crinkly texture, and in some places, individual branches (possibly of coralline algae or bryozoans) can be identified in the SAS images (see Supplement 1, Figure S1-5), suggesting extensive biofouling of all available hard substrate.

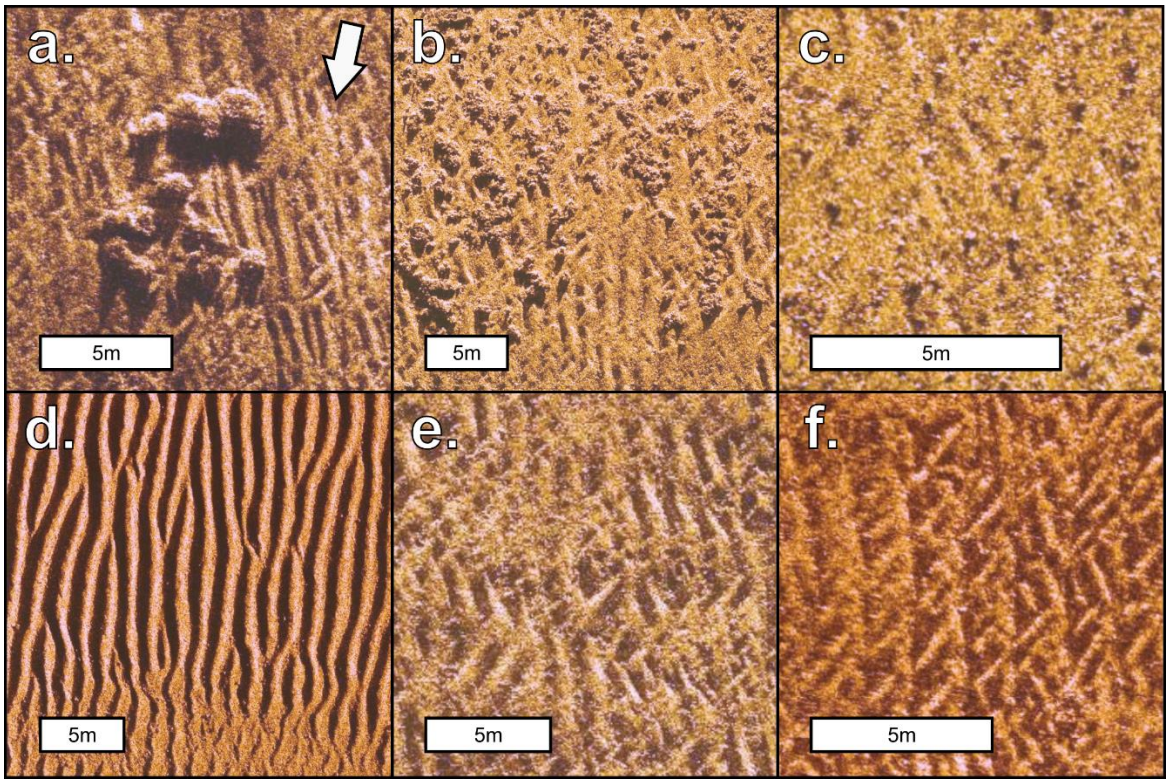

Figure 4: Representative SAS imaging of the seafloor features: a. large solitary bioconstructions (boulder size); b. intermediate bioconstructions; c. small bioconstruction or rocks, suspected as rhodoliths; d. linear bedforms; e. chevron bedforms; f. super position of chevron bedforms atop linear bedforms. All scale bars are 5m, arrow in a shows illumination direction.

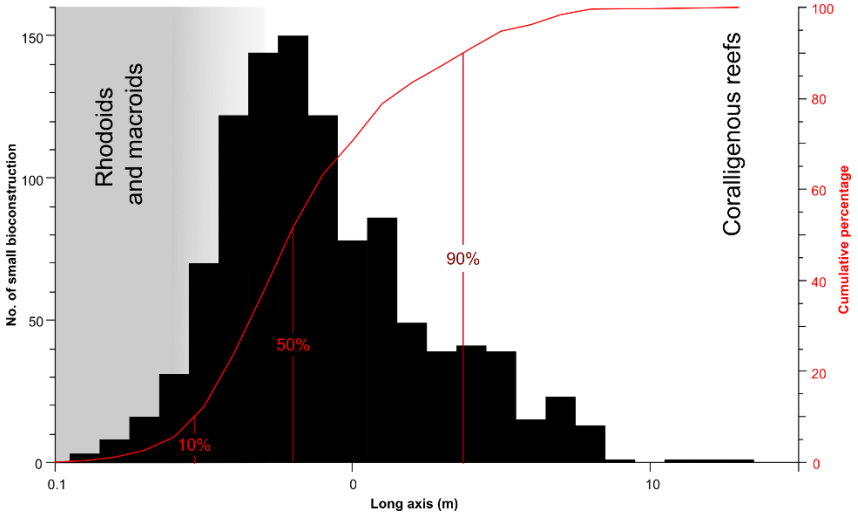

Figure 5: Long axis size distribution (log scale) of rocks/bioconstructions sampled from the SAS imaging (n=1053), vertical lines denotes the percentile fractions.

Bedforms range in axis lengths from ~0.3m to 70m and wavelength from ~0.2m to ~7m (Figure 6a). Bedforms occur in three principal forms: large linear bedforms (Figure 4d), short chevron bedforms (Figure 4e) and superposition of the two (Figure 4f). The linear bedforms are aligned primarily with a north-south bearing axis; these bedforms may reach up to 70m along their long axis (Figure 6b), but for the most part exhibit a maximum wavelength of up to 2m. The chevron bedforms are shorter, with axes bearing to the northwest-southeast or northeast-southwest (Figure 6c). At times, chevron bedforms are observed superimposed on the linear bedforms (Figure 4f), whereas, in a few cases, they occur as poorly developed ladder-like bedforms (small bedforms linking adjacent larger ones) in between the linear bedforms. The chevron bedforms extend to a maximum length of ~15m but may have a wavelength of up 7m. The bedforms are generally concentrated in stretches along the valleys and up the south-facing slopes of the ridges (Figures 7a, b, 8a). The linear bedforms occur primarily in the southern margins of the valley, while the chevron bedform occurs primarily in the northern margin. However, the chevron and mixed bedforms can also occur in the south of the valleys, notably if they are very small. Transition between chevron and linear bedforms appear to occur with increase of thickness of the sediment (Figure 8b, c). The chevron bedform are present in thinner sediment fill while the linear bedforms corresponds to thicker sediment fill. There is no clear correlation between the wavelengths and bedform axis lengths ($r=0.19$, $n=5143$; Figure 6d) nor is there one between either of them and the bearing ($r=-0.01$, $n=5143$ and $r=0.01$, $n=8324$, respectively). However, the relation between bedform wavelengths and bedform axis lengths may show two trends with a gradient between them: a long axis / short wavelength cluster, which is mainly associated with linear bedforms, and a long wavelength / short axis cluster, which is mainly chevron associated with bedforms,. The wavelengths do not change spatially along any clear gradient, although there is a slight increase in axis lengths to the southwest. On a smaller scale, the wavelengths seem to exhibit some interaction with the seafloor geometry, such a decrease in wavelength with increased slope (Figure 7b), but this was not consistent spatially in a quantifiable way.

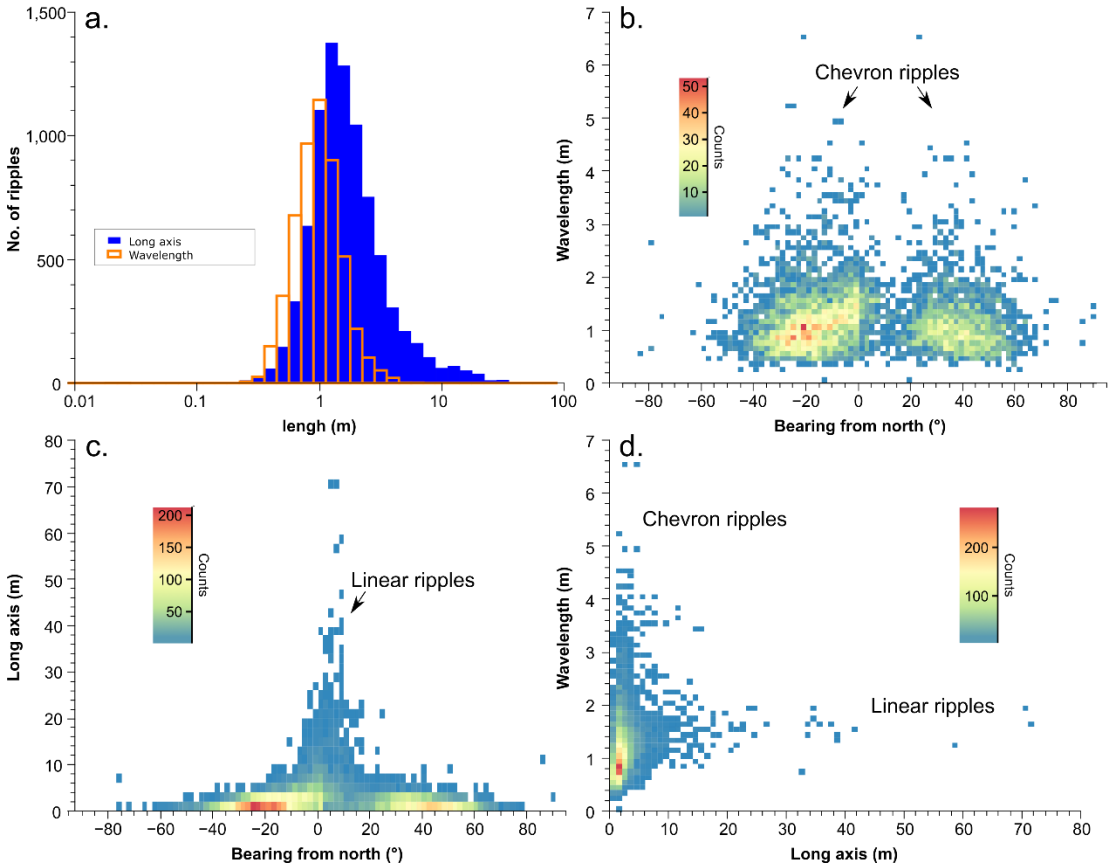

Figure 6: Bedform characteristics: a. distribution of long axis length (n=8323) and bedform wavelength (n=3557); b. relation between bearing and wavelength; c. relation between long axis length and bearing; d. relation between wavelength and long axis length.

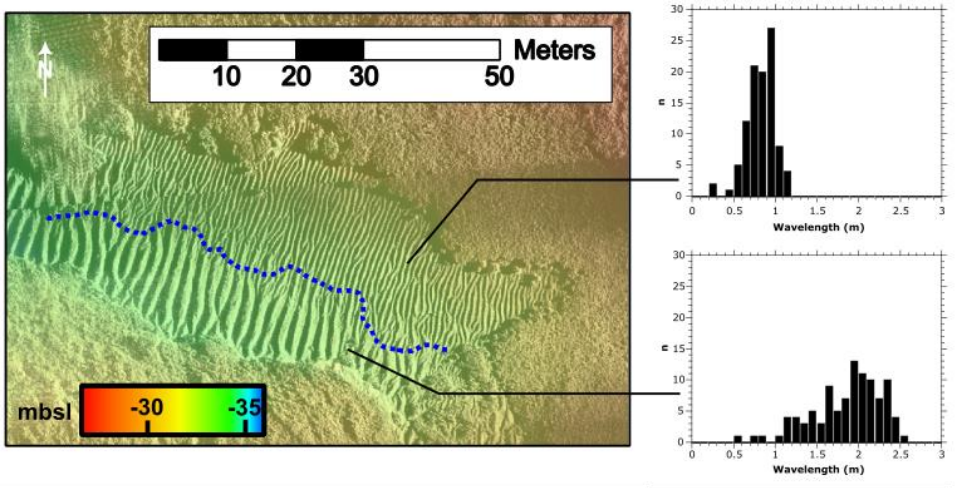

Figure 7: Relation between bathymetry and bedform morphology. Interlaced seafloor SAS seafloor image and bathymetry (note slope is steeper south of the line), blue dashed line marks the transition in bedform morphology. Histograms (n=100) shows the change in wavelength on either side of the dashed blues line.

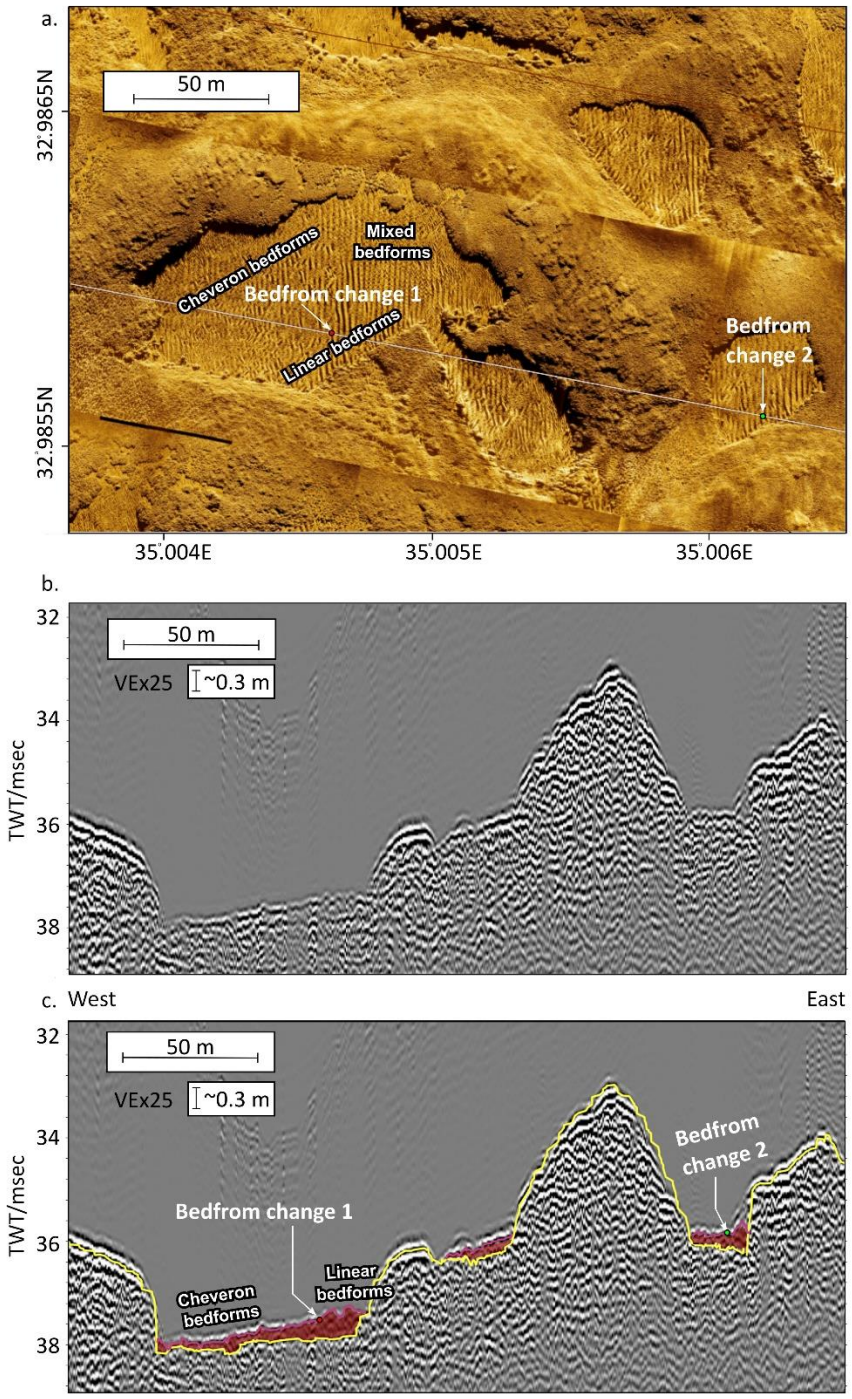

Figure 8: Seismic line across the sedimentary fill of the valleys, a. SAS imaging of the seafloor along the seismic line, the transition from chevron to linear bedforms marked. b. uninterpreted seismic imaging. c. interpreted seismic imaging showing the sedimentary fill (red) and the top of the rock surface (yellow).

Sedimentary Description

The SBP profiles reveal that the main Bustan HaGalil Ridge structure bedrock is buried in its peripheries by sub-meter scale layered sediments, with their thickness increasing outwards to several meters (Figure 9). Some of the buried ridge peaks outcrop as solitary rocky elements at the modern seafloor with biological cover. Northward directed moats are formed behind the edges of the ridges and the solitary rocks and sediment pileup are observed on southern flanks of such obstacles (Figure 9a). Together, these point to a northward current driven sediments transport. The layered sediments exhibit onlap patterns (Figure 9b), at times leaning against the ridges at a slight angle. Evidence for scouring appear also in the SBP images of the sub-surface, showing distorted and mounded layering in the vicinity of some of the ridge promontories (Figure 9b, c). These appear in the uppermost (youngest) layers, as well as in some of the deeper (older) levels . At a smaller scale, some changes in bedform character is observed between south and north of the solitary rocks (Figure 10a, b). However, the biogenic cover of the rocks (Figure 10b) does not exhibit any clear directional features. The biogenic cover appears to be a meshwork of encrusting algae, foraminifera and other organisms, which can be classified as coralligenous (See also Supplement 1, Figure S1-2).

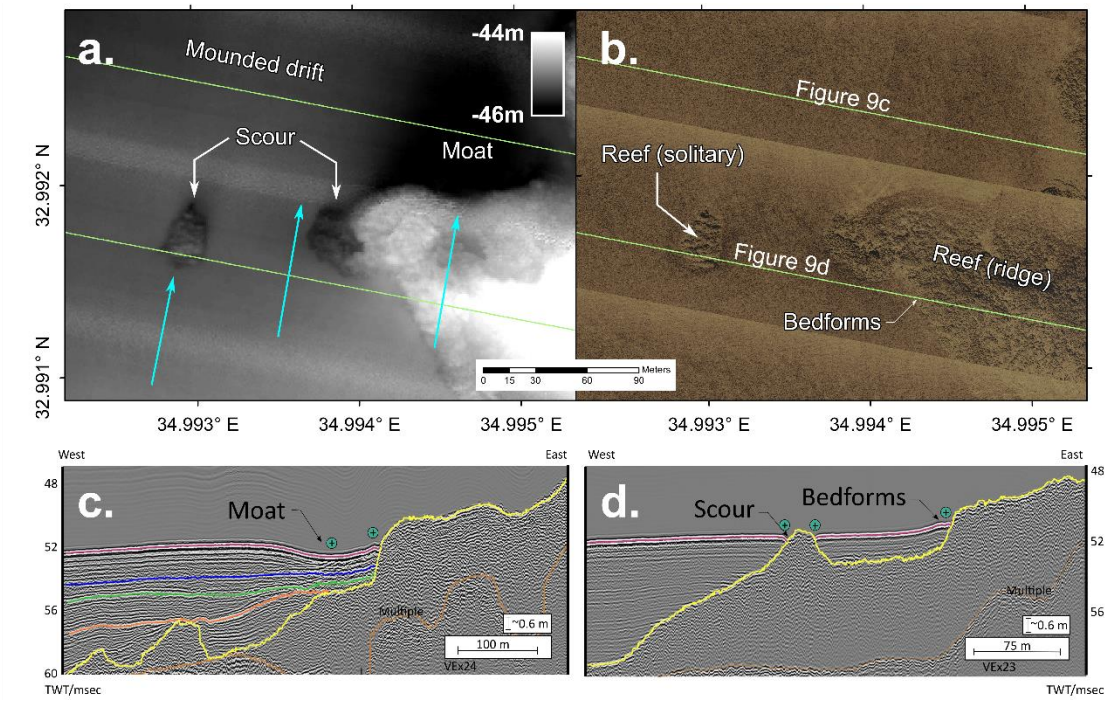

Figure 9: Character of the fill on the western flank of the Bustan HaGalil ridge. a. bathymetric and b. SAS image on the bathymetry showing the location of the seismic lines and inferred current direction. c. interpreted seismic imaging showing the northern line. d. interpreted seismic imaging showing the southern line.

In contrast to the layered sediments around the Bustan Hagalil Ridge, the bedform patches within the Ridge's valleys comprise a relatively thin sedimentary fill, overlying the bedrock (Figure 8). This sediments fill has a maximum thickness of ~0.6msec (~0.5m assuming velocity of 1500 m/sec) and is only a few cm thick in places. With an increase of thickness, the bedform character changes from chevron bedforms to linear bedforms (Figure 8a, c). The sediments collected and photographed in the field (Figure 10c, d) exhibit a grain size range between coarse sand and coarse gravel (calcarenite to calcirudite *sensu* Grabau, 1904) with most of the grains in the fine to medium gravel range. Analysis dive photographs reveals coarser grains in the troughs and finer at the crests of the bedforms (Figure 10c). In dive photography (Figure 10d, e; see also Supplement 1 Figure S1-2) and hand sample, the sediment is composed primarily of coralline algae nodules with other bioclastic fragments a few mm to cm in size. The nodules are brown, black or yellowish red, rounded, elongating and irregular in shape, ranging in size between few mm to few cm. Most of the coralline algae in the nodules appears to be dead (at the time and location of collection), based on the color and presence of encrustation on some of the nodules. Encrusts present are mainly by bryozoans, although serpulids or other vermiforms are observed as well as possibly encrusting foraminifera (*Miniacina sp.* or *Homotrema sp.*). The bioclastics fragments include bivalves, gastropods, serpulids (or vermetid), echinoderms and bryozoans, individual coral polyps were also found present. Bryozoan fragments of multiple morphologies, including benching and encrusting forms, are common. A few larger benthic foraminifera are present, mainly *Amphistegina spp.* (invasive species). Mineralogically the sediment is comprised of high magnesium calcite and a smaller fraction of aragonite, consistent with the observed clades.

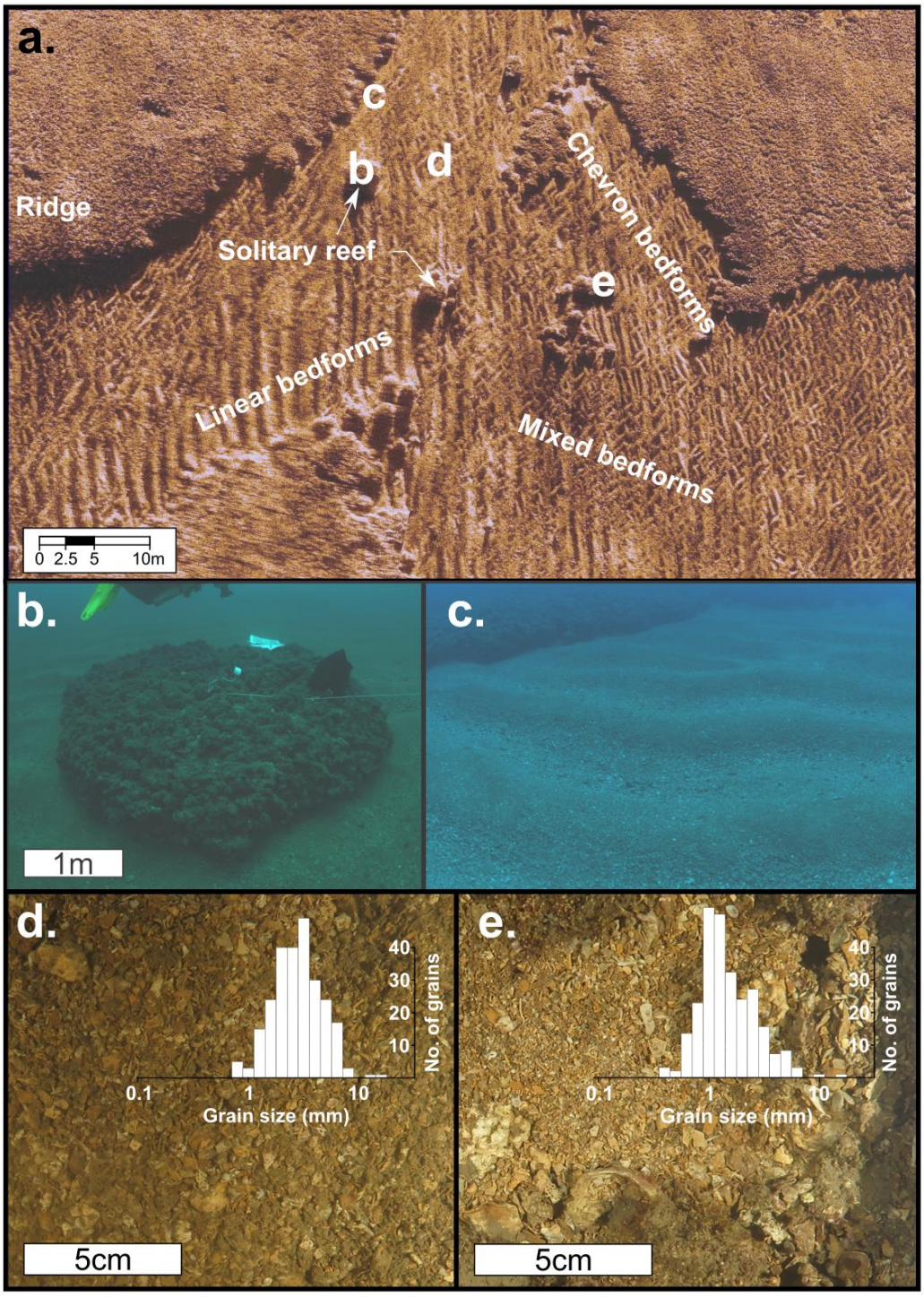

Figure 10: a. Configuration of bedform elements within a small valley, showing all types of bedforms in one locations and positions of subfigures b to e. b. solitary reef/bioconstruction of encrusting organisms, notably coralline algae. c. individual bedforms at the base of the ridge. d. sediment and grain size distribution in the mixed ripples bedforms. e. sediment and grain size distribution in the chevron ripples bedforms.

Local wind and wave character

For surface waves, both dominant period and significant wave height in the Galilee shelf exhibit a log-normal distribution, with a log mean of 0.7±0.2 (4.8m) and -0.3±0.3 (0.5m), respectively (n=18841 for both). Mean period is closer to normal distribution with a mean of 3.7±0.7m. Calculating the wavelength from the mean period (Figure 11, see also Supplementary Material), results in a mean wavelength of 22.5±9.6m (n=18686) and a $\tilde{\mu}_3$=1.8, the 10th percentile of 13.9m, 90th percentile of 35.4m, and a maximum wavelength of 84m. This would translate to a wave base shallower then 18m for more than 90% of waves and only 1% reaching the depths of sediment bedforms observed in the study area.

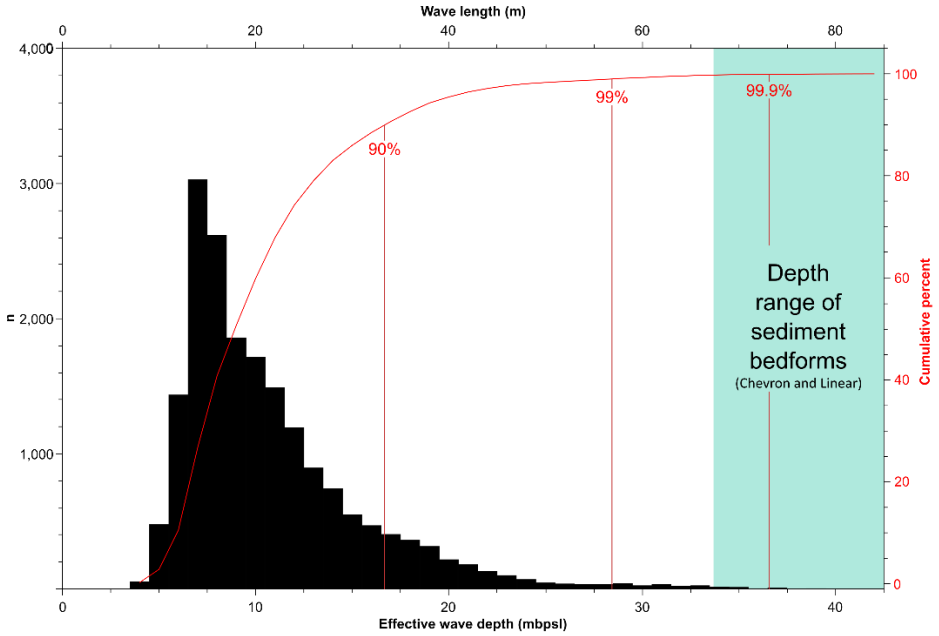

Figure 11: Wavelength distribution based on the THEMO1 data, blue area marks the effected depth range in the study area.

Brunt–Väisälä frequency distribution exhibit low values (1.6±2.3 cycles/hour, $\tilde{\mu}_3$=1.2, n=563) during winter and spring months (December to April). In summer and autumn months (May to October) values increase (5.9±5.5 cycles/hour, $\tilde{\mu}_3$=0.5, n=851). The highest frequencies (>25 cycles/hour) are located between 20 and 80 mbsl, with two main peaks (Figure 12) 20 to 30 mbsl and 60 to 70 mbsl. High frequencies persist between these two peaks representing the migration of the pycnocline through the warm summer-autumn periods (Figure 1c). These values and distribution are comparable to previously published values for the southern Israeli shelf (Reiche et al., 2018).

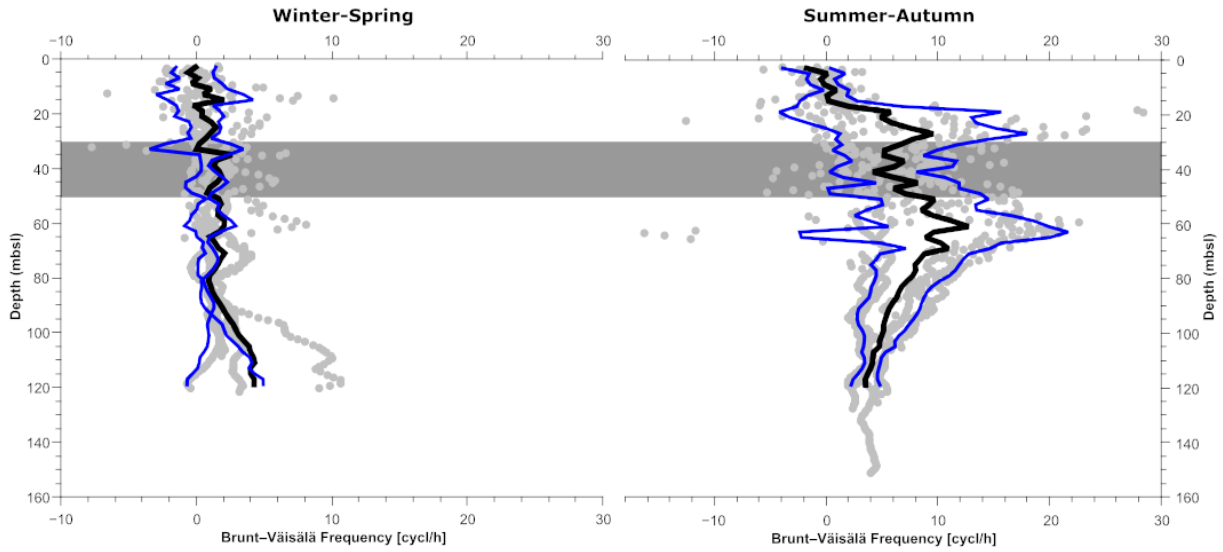

Figure 12: Distribution of Brunt–Väisälä frequencies in the water column during winter-spring and summer-autumn (see Figure 1c for density distribution for each month).

DISCUSSION

The Bustan HaGalil ridge forms an elevated structure in the middle of the northern Israeli shelf. The elevated parts of this structure offer a hard substrate on which recruitment can occur for the various calcifying groups present in the Eastern Mediterranean. These groups include coralline algae, hydrozoan, bryozoans, sponges, larger benthic foraminifera, molluscs and potentially some corals (Albano et al., 2020; Cerrano et al., 2019; Corriero et al., 2019; Goren et al., 2021; Idan et al., 2018). Remains of many of these groups are present in the sediment found in valleys of the Bustan HaGalil ridge (Figure 10b-e). The binding, encrustation and accumulation of these organisms results in the development of extensive coralligenous bioconstruction atop the original hard surface. These group and construction are similar those described in mesophotic reefs and biogenic buildups in the central Mediterranean (Bialik et al., 2022; Ingrosso et al., 2018). The initial geometries of these buildup is at time inheriting from underlying Pleistocene strata (Varzi et al., 2023) and local sediment distribution patterns (Sherman et al., 2019). That said, farther development of the biological cover would be the product of local oceanographic conditions. Most Pleistocene beach ridges in the region are oriented north-south (Mauz et al., 2013), whereas the internal ridges are originated east-west (Figure 2d). They are also asymmetric along the north-south axis. This would suggest their modern geometry had developed during the Holocene, interacting with oceanographic conditions.

The biogenic grains that form the sedimentary fill between the ridges, comprised of the same groups present in the build-ups, are locally produced. The production of most of these components probably occurs predominantly on the highs and is then transported to the lower areas by current and gravity. One exception to this may be some coralline algae, as nodules are present in the sediment. Given the abundance of coralline nodules in the sediment, prior description of large rhodoliths in this region of the Israeli shelf (Dulin et al., 2020) and the size distribution (Figure 5) the smaller rocky elements are considered rhodoliths (Figure 4c). Coralline algae can coat on mobile substrate, and as such their fragmentation from crust can also lead to their transformation into nodules as they circulate by currents and animals (Braga and Martín, 1988). The production is most likely local and limited due to high stress and low nutrient availability in the region (Krom et al., 2005; Ozer et al., 2017; Thingstad et al., 2005). A limited production potential partially explains the minimal fill of the available relief (Figure 8c).

Mesophotic reefs are usually removed from resuspension by fair-weather waves (Baker et al., 2016). Meanwhile, lateral transport is of greater importance in mesophotic settings than deposition from the water column (Sherman et al., 2016). This redistribution of material impacts the lateral and vertical physical growth of the reef as well as the ecosystem that inhabits it, as is often the case in shallow water reefs (Hernández et al., 2009; Storlazzi et al., 2004).

The variation in bedform geometry, shape and orientation suggests more than one sediment dispersal system at play. The moat and mound geometry (Figure 9) is indicative of mounded drift (Faugères et al., 1999; Miramontes et al., 2021; Nielsen et al., 2008; Paulat et al., 2019), indicating an active bottom current system oriented parallel to the shelf, flowing from south to north. This would be consistent with the south-north direction of bottom currents described in other areas of the Israeli shelf (Schattner, 2021; Schattner et al., 2015). This is most visible outside of the ridge. There the supply of sediment from the south overwhelms the biogenic production, as suggested by the difference is sediment thickness in the ridge's valleys (Figure 8c) and to the west of the ridge (Figure 9 b & c).

The south to north direction would also fit the asymmetry of the ridges and would suggest a relation. This transport mode was not clearly identified within the Bustan HaGalil Ridge but is consistent with the direction of linear bedforms (Figure 6c). The presence of sediment on the southern side (Figure 7b), possibly pushed by the current is a secondary line of evidence and may be a factor leading to the asymmetry. The change in linear bedform wavelength with slope (Figure 7) could then be explained by the difference in the angle of contact between the current and the seafloor. The focusing of the contour currents through the gaps of the ridge should also result in a delta drift (Lüdmann et al., 2018) like

geometries, but these were not clearly observed in the data. The current may also play a critical role in supplying nutrients, leading to differential biogenic growth rates on the south and north aspects of the ridges. Rare storm waves (Figure 11) may also impact these regions, but no clear evidence of these was identified in the surveys, which were carried out in summer.

The mechanism generating the chevron bedforms is not as straightforward. The bedforms are below the fair wave base and even marginally affected by storm waves (Figure 11). This excludes the possibility that these bedforms are the product of wind-driven waves. Moreover, these features are primarily found within the valleys and at time superimposed on the linear bedforms. This suggests that either the mechanism is not spatially uniform and differs from the bottom currents generating the linear bedforms, or is not temporally uniform. Since the chevron bedforms are superimposed on the linear bedforms (Figures 4f, 10a), it is possible that the linear bedforms formed first, the mechanism controlling them subsided and then the one generating the chevron bedforms initiated. The alternation between the two modes might be seasonally or on longer time scale. Alternatively, both mechanisms might be at play, but at different intensities in space.

Based on the depth and spatial distribution of these features, we propose that they are the product of refracted internal waves. The Brunt–Väisälä frequency distribution (Figure 12) indicates that the internal wave propagation in the depth range in which these bedforms occur is likely. This will be especially true during the summer-autumn period when the water body is stratified. As such, the internal waves might be a more prominent component during summer while shelf parallel currents are more prominent during winter when the pycnocline is shallower.

Features generated by internal waves elsewhere on the Israeli shelf exhibit wavelengths in the range of 10s to 100s of meters (Reiche et al., 2018). This stands in contrast to decimetres to single meters observed here with the benefit of higher resolution from SAS. Features of similar magnitude might have been missed due to limitation of the imaging technology. But there is argument that the generation mechanism and wavelength of the internal waves at play are the cause of the difference. Deeper internal waves have low-frequency and the features generated by them over long term processes would be larger. Meanwhile internal waves generated at shallower depth can be the product of resonance with the surface waves and thus have a higher frequency (Olbers and Eden, 2016). The presence of multiple domains and frequencies of internal waves in this region is related to the local structure of the water column, notably the development of a strong pycnocline during summer (Figure 1c). This pycnocline is not depth static and

oscillates in depth and intensity through the year. As such, its ability to carry internal waves is not consistent and adds to multiple energy states then interacting with the seafloor.

The orthogonal relationship of the chevron bedforms and their location within the valleys (with preference to the north, Figure 10a) suggests that the waves at play are not only free water waves. Currents may play a role in modulating the wave propagation, but the principle south-north current appears to be more conducive to the formation of the linear bedforms. The confines of the valleys and the multiple obstacles in them and around them could result in wave reflection and refraction, which are known to define sediment distribution around reefs (Mandlier and Kench, 2012). While there is random orientation, the preference of two main directions in the chevron bedforms (Figure 6b) suggests that there is some constructive and destructive interference of the refracted waves at certain angles. These interferences could occur either with refracted waves themselves or with the incoming waves. This interference may also modify the apparent frequency and shape of the internal wave interacting with the sediment (Badiey et al., 2011; Oba and Finette, 2002). To the west of the ridge, where external currents are more powerful, the impact of the interval waves is significantly reduced. Strong currents diminish the impact of internal waves (Stastna and Lamb, 2008), leading to the formation of mound and moat features (Figure 13).

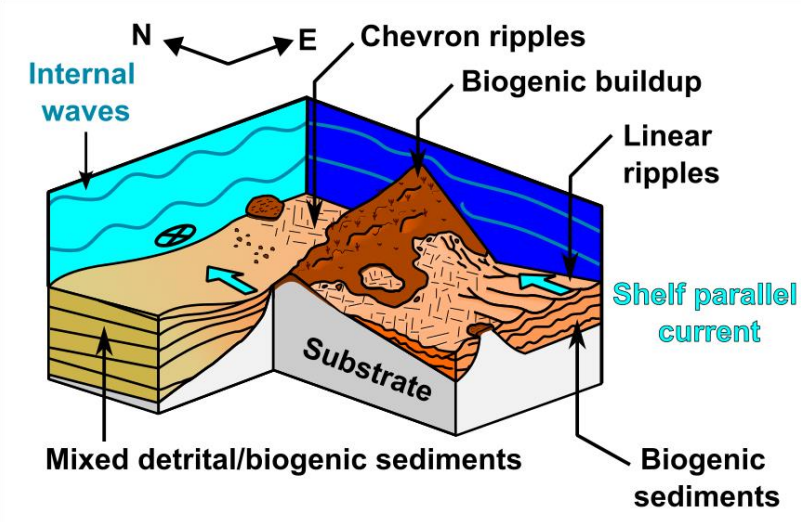

Figure 13: Schematic model (not to scale) of the configuration and process at play in the Bustan HaGalil ridge.

The findings from Bustan Ha Galil do support the argument that internal waves play a role in modulating turbidity and sediment distribution in mesophotic settings (Pomar et al., 2012). However, they are not the only mechanism at play in this environment. Inferring from the size of bedforms, the linear bedforms and drift bodies are significantly larger than the chevron bedforms. This indicates that bottom currents are a

more powerful seafloor shaping mechanism than the internal waves (Bartholdy et al., 2005), at least in this location. Moreover, while coralline algae nodules require only slight agitation (Marrack, 1999), the grain size of the sediment (Figure 10d, e) suggests significant transport energy. Field relations, notably the existence of the mixed bedforms, suggest that the shaping mechanisms vary spatially. Were only the currents at play, they would result in seafloor repavement which leaves only the linear bedforms (Figure 13). This might happen in locations where the sediment accumulated vertically (Figure 8a, c), elevating it from local obstructions. Interactions between these two transport mechanisms shapes the sediment distribution here. In other locations, where bottom currents are weaker and internal waves are stronger, the latter may play a more significant role and possibly generate local currents (Mandlier and Kench, 2012). This interaction is likely also a major player in shaping the coralligenous buildups and modulating their growth.

CONCLUSIONS

Mesophotic reefs are an important but still underexplored marine niche that may become even more important with warming of the surface ocean (Lesser et al., 2018). Sediment distribution in these settings is still very poorly understood. Here we carried out high-resolution imaging acoustic imaging of a mesophotic case study in the southeastern Mediterranean Sea. We observed a mosaic of hard substrate reefs and maerl (rhodolith) beds interspersed with locally produced, coarse grained, biogenic sediment. These sediments are redistributed by bottom currents and, to a lesser extent, internal waves (Figure 13). The interactions between these two transport mechanisms shape the bedforms present in this setting.

The full role of internal waves in the mesophotic setting is still far from fully understood. These findings highlight the complex nature of this system and the need for more detailed work. Implementation of high-resolution imaging solution with large spatial coverage, be them acoustic or photogrammetry, in other mesophotic settings is needed to improve our understanding of the dynamics in and around them.

ACKNOWLEDGEMENTS

This study was conducted as part of the first author's Marie Skłodowska Curie fellowship (101003394 — RhodoMalta). OMB is currently supported by the German (GEOMAR) - Israeli (University of Haifa) Helmholtz International Laboratory: The Eastern Mediterranean Sea Centre - An Early-Warning Model-System for our Future Oceans (EMS FORE). Financial support for this work was provided by a grant from the Yad Hanadiv charitable trust to YM. Our thanks to the technical diving team of the Morris Kahn Marine Research Station for aid in sample and data collection.

Data Availability

All supplementary and ancillary data is available via Figshare at 10.6084/m9.figshare.19642449 (https://figshare.com/s/6165f5654b4fb00183e7).

REFERENCES

Albano, P.G., Azzarone, M., Amati, B., Bogi, C., Sabelli, B., Rilov, G., 2020. Low diversity or poorly explored? Mesophotic molluscs highlight undersampling in the Eastern Mediterranean. Biodivers. Conserv. 29, 4059–4072. https://doi.org/10.1007/s10531-020-02063-w

Alhammoud, B., Béranger, K., Mortier, L., Crépon, M., Dekeyser, I., 2005. Surface circulation of the Levantine Basin: Comparison of model results with observations. Prog. Oceanogr. 66, 299–320. https://doi.org/10.1016/j.pocean.2004.07.015

Allen, J.R.L., 1985. Principles of physical sedimentology. Chapman and Hall, London. https://doi.org/10.1007/978-94-010-9683-6

Almagor, G., Gill, D., Perath, I., 2000. Marine Sand Resources Offshore Israel. Mar. Georesources Geotechnol. 18, 1–42. https://doi.org/10.1080/10641190009353781

Almogi-Labin, A., Calvo, R., R., H.E., Amit, R., Harlavan, Y., Herut, B., 1The, 2012. Sediment Characterisation of the Israeli Mediterranean Shelf (10-100 m). Jerusalem.

Amado-Filho, G.M., Moura, R.L., Bastos, A.C., Francini-Filho, R.B., Pereira-Filho, G.H., Bahia, R.G., Moraes, F.C., Motta, F.S., 2016. Mesophotic ecosystems of the unique South Atlantic atoll are composed by rhodolith beds and scattered consolidated reefs. Mar. Biodivers. 46, 933–936. https://doi.org/10.1007/s12526-015-0441-6

Badiey, M., Katsnelson, B.G., Lin, Y.-T., Lynch, J.F., 2011. Acoustic multipath arrivals in the horizontal plane due to approaching nonlinear internal waves. J. Acoust. Soc. Am. 129, EL141–EL147. https://doi.org/10.1121/1.3553374

Baker, E., Puglise, K.A., Colin, P., Harris, P.T., Kahng, S.E., Rooney, J.J., Sherman, C., Slattery, M., Spalding, H., 2016. What are mesophotic coral ecosystems?, in: Baker, E.K., Puglise, K.A., Harris, Peter T (Eds.), Mesophotic Coral Ecosystems—a Lifeboat for Coral Reefs? The United Nations Environment Programme and GRID-Arendal, Nairobi, pp. 11–19.

Bartholdy, J., Flemming, B.W., Bartholomä, A., Ernstsen, V.B., 2005. Flow and grain size control of depth-independent simple subaqueous dunes. J. Geophys. Res. Earth Surf. 110, n/a-n/a. https://doi.org/10.1029/2004JF000183

Bialik, O.M., Varzi, A.G., Durán, R., Le Bas, T., Gauci, A., Savini, A., Micallef, A., 2022. Mesophotic Depth Biogenic Accumulations ("Biogenic Mounds") Offshore the Maltese Islands, Central Mediterranean Sea. Front. Mar. Sci. 9. https://doi.org/10.3389/fmars.2022.803687

Bianchi, Carlo, N., Morri, C., 2003. Global sea warming and "tropicalisation" of the Mediterranean Sea: biogeographic and ecological aspects. Biogeogr. – J. Integr. Biogeogr. 24. https://doi.org/10.21426/B6110129

Boegman, L., Ivey, G.N., 2009. Flow separation and resuspension beneath shoaling nonlinear internal waves. J. Geophys. Res. Ocean. 114, 1–15. https://doi.org/10.1029/2007JC004411

Bongaerts, P., Frade, P.R., Ogier, J.J., Hay, K.B., van Bleijswijk, J., Englebert, N., Vermeij, M.J., Bak, R.P., Visser, P.M., Hoegh-Guldberg, O., 2013. Sharing the slope: depth partitioning of agariciid corals and associated Symbiodinium across shallow and mesophotic habitats (2-60 m) on a Caribbean reef. BMC Evol. Biol. 13, 205. https://doi.org/10.1186/1471-2148-13-205

Bradford, J.M., Chang, F.H., 1987. Standing stocks and productivity of phytoplankton off Westland, New Zealand, February 1982. New Zeal. J. Mar. Freshw. Res. 21, 71–90. https://doi.org/10.1080/00288330.1987.9516202

Braga, J.C., Martín, J., 1988. Neogene coralline-algal growth-forms and their palaeoenvironments in the Almanzora river valley (Almeria, S.E. Spain). Palaeogeogr. Palaeoclimatol. Palaeoecol. 67, 285–303. https://doi.org/10.1016/0031-0182(88)90157-5

Brokovich, E., Einbinder, S., Shashar, N., Kiflawi, M., Kark, S., 2008. Descending to the twilight-zone: changes in coral reef fish assemblages along a depth gradient down to 65 m. Mar. Ecol. Prog. Ser. 371, 253–262. https://doi.org/10.3354/meps07591

Cacchione, D.A., 1970. Experimental study of internal gravity waves over a slope. Massachusetts Institute of Technology and Woods Hole Oceanographic Institution, Woods Hole, MA. https://doi.org/10.1575/1912/1348

Cacchione, D.A., Drake, D.E., 1986. Nepheloid layers and internal waves over continental shelves and

slopes. Geo-Marine Lett. 6, 147–152. https://doi.org/10.1007/BF02238085

Cerrano, C., Bastari, A., Calcinai, B., Di Camillo, C., Pica, D., Puce, S., Valisano, L., Torsani, F., 2019. Temperate mesophotic ecosystems: gaps and perspectives of an emerging conservation challenge for the Mediterranean Sea. Eur. Zool. J. 86, 370–388. https://doi.org/10.1080/24750263.2019.1677790

Cheriton, O.M., McPhee-Shaw, E.E., Shaw, W.J., Stanton, T.P., Bellingham, J.G., Storlazzi, C.D., 2014. Suspended particulate layers and internal waves over the southern Monterey Bay continental shelf: An important control on shelf mud belts? J. Geophys. Res. Ocean. 119, 428–444. https://doi.org/10.1002/2013JC009360

Church, J.A., Andrews, J.C., Boland, F.M., 1985. Tidal currents in the central Great Barrier Reef. Cont. Shelf Res. 4, 515–531. https://doi.org/10.1016/0278-4343(85)90008-1

Clifton, H.E., Dingler, J.R., 1984. Wave-Formed Structures and Paleoenvironmental Reconstruction. Mar. Geol. 60, 165–198. https://doi.org/10.1016/S0070-4571(08)70146-8

Corriero, G., Pierri, C., Mercurio, M., Nonnis Marzano, C., Onen Tarantini, S., Gravina, M.F., Lisco, S., Moretti, M., De Giosa, F., Valenzano, E., Giangrande, A., Mastrodonato, M., Longo, C., Cardone, F., 2019. A Mediterranean mesophotic coral reef built by non-symbiotic scleractinians. Sci. Rep. 9, 3601. https://doi.org/10.1038/s41598-019-40284-4

Davis, K.A., Monismith, S.G., 2011. The modification of bottom boundary layer turbulence and mixing by internal waves shoaling on a barrier reef. J. Phys. Oceanogr. 41, 2223–2241. https://doi.org/10.1175/2011JPO4344.1

Dulin, T., Avnaim-Katav, S., Sisma-Ventura, G., Bialik, O.M., Angel, D.L., 2020. Rhodolith beds along the southeastern Mediterranean inner shelf: Implications for past depositional environments. J. Mar. Syst. 201. https://doi.org/10.1016/j.jmarsys.2019.103241

Faugères, J.-C., Stow, D.A.., Imbert, P., Viana, A., 1999. Seismic features diagnostic of contourite drifts. Mar. Geol. 162, 1–38. https://doi.org/10.1016/S0025-3227(99)00068-7

Goren, L., Idan, T., Shefer, S., Ilan, M., 2021. Macrofauna Inhabiting Massive Demosponges From Shallow and Mesophotic Habitats Along the Israeli Mediterranean Coast. Front. Mar. Sci. 7, 612779. https://doi.org/10.3389/fmars.2020.612779

Grabau, A.W., 1904. On the Classification of Sedimentary Rocks. Wentworth Press.

Grossowicz, M., Bialik, O.M., Shemesh, E., Tchernov, D., Vonhof, H.B., Sisma-Ventura, G., 2020. Ocean warming is the key filter for successful colonisation of the migrant octocoral Melithaea erythraea (Ehrenberg, 1834) in the Eastern Mediterranean Sea. PeerJ 8, e9355. https://doi.org/10.7717/peerj.9355

Hernández, R., Sherman, C., Weil, E., Yoshioka, P., 2009. Spatial and temporal patterns in reef sediment accumulation and composition, southwestern insular shelf of Puerto Rico. Caribb. J. Sci. 45, 138–150. https://doi.org/10.18475/cjos.v45i2.a3

Idan, T., Shefer, S., Feldstein, T., Yahel, R., Huchon, D., Ilan, M., 2018. Shedding light on an East-Mediterranean mesophotic sponge ground community and the regional sponge fauna. Mediterr. Mar. Sci. 19, 84. https://doi.org/10.12681/mms.13853

Ingrosso, G., Abbiati, M., Badalamenti, F., Bavestrello, G., Belmonte, G., Cannas, R., Benedetti-Cecchi, L., Bertolino, M., Bevilacqua, S., Bianchi, C.N., Bo, M., Boscari, E., Cardone, F., Cattaneo-Vietti, R., Cau, A., Cerrano, C., Chemello, R., Chimienti, G., Congiu, L., Corriero, G., Costantini, F., De Leo, F., Donnarumma, L., Falace, A., Fraschetti, S., Giangrande, A., Gravina, M.F., Guarnieri, G., Mastrototaro, F., Milazzo, M., Morri, C., Musco, L., Pezzolesi, L., Piraino, S., Prada, F., Ponti, M., Rindi, F., Russo, G.F., Sandulli, R., Villamor, A., Zane, L., Boero, F., 2018. Mediterranean Bioconstructions Along the Italian Coast. Adv. Mar. Biol. 78, 61–136. https://doi.org/10.1016/bs.amb.2018.05.001

James, N.P., Collins, L.B., Bone, Y., Hallock, P., 1999. Subtropical carbonates in a temperate realm; modern sediments on the Southwest Australian shelf. J. Sediment. Res. 69, 1297–1321. https://doi.org/10.2110/jsr.69.1297

James, N.P., Lukasik, J.J., 2010. Cool- and cold-water neritic Carbonates, in: James, N.P., Dalymple, R.W. (Eds.), Facies Models 4. Geolocial Association of Canada, St. John, pp. 371–399.

Kahng, S., Copus, J., Wagner, D., 2014. Recent advances in the ecology of mesophotic coral ecosystems (MCEs). Curr. Opin. Environ. Sustain. 7, 72–81. https://doi.org/10.1016/j.cosust.2013.11.019

Kahru, M., 1983. Phytoplankton Patchiness Generated by Long Internal Waves: A Model. Mar. Ecol. Prog. Ser. 10, 111–117.

Kress, N., Herut, B., 2001. Spatial and seasonal evolution of dissolved oxygen and nutrients in the Southern Levantine Basin (Eastern Mediterranean Sea): chemical characterisation of the water masses and inferences on the N:P ratios. Deep Sea Res. Part I Oceanogr. Res. Pap. 48, 2347–2372. https://doi.org/10.1016/S0967-0637(01)00022-X

Krom, M.D., Woodward, E.M.S., Herut, B., Kress, N., Carbo, P., Mantoura, R.F.C., Spyres, G., Thingstad, T.F., Wassmann, P., Wexels-Riser, C., Kitidis, V., Law, C.S., Zodiatis, G., 2005. Nutrient cycling in the south east Levantine basin of the eastern Mediterranean: Results from a phosphorus starved system. Deep Sea Res. Part II Top. Stud. Oceanogr. 52, 2879–2896. https://doi.org/10.1016/j.dsr2.2005.08.009

Lamb, K.G., 2014. Internal wave breaking and dissipation mechanisms on the continental slope/shelf. Annu. Rev. Fluid Mech. 46, 231–254. https://doi.org/10.1146/annurev-fluid-011212-140701

Laverick, J.H., Tamir, R., Eyal, G., Loya, Y., 2020. A generalised light-driven model of community transitions along coral reef depth gradients. Glob. Ecol. Biogeogr. 29, 1554–1564. https://doi.org/10.1111/geb.13140

Leichter, J.J., Shellenbarger, G., Genovese, S.J., 1998. Breaking internal waves on a Florida (USA) coral reef: a plankton pump at work? . Mar. Ecol. Prog. Ser. 166, 83–97.

Lesser, M.P., Slattery, M., Leichter, J.J., 2009. Ecology of mesophotic coral reefs. J. Exp. Mar. Bio. Ecol. 375, 1–8. https://doi.org/10.1016/j.jembe.2009.05.009

Lesser, M.P., Slattery, M., Mobley, C.D., 2018. Biodiversity and Functional Ecology of Mesophotic Coral Reefs. Annu. Rev. Ecol. Evol. Syst. 49, 49–71. https://doi.org/10.1146/annurev-ecolsys-110617-062423

Lüdmann, T., Betzler, C., Eberli, G.P., Reolid, J., Reijmer, J.J.G., Sloss, C.R., Bialik, O.M., Alvarez-Zarikian, C.A., Alonso-García, M., Blättler, C.L., Guo, J.A., Haffen, S., Horozal, S., Inoue, M., Jovane, L., Kroon, D., Lanci, L., Laya, J.C., Mee, A.L.H., Nakakuni, M., Nath, B.N., Niino, K., Petruny, L.M., Pratiwi, S.D., Slagle, A.L., Su, X., Swart, P.K., Wright, J.D., Yao, Z., Young, J.R., 2018. Carbonate delta drift: A new sediment drift type. Mar. Geol. 401. https://doi.org/10.1016/j.margeo.2018.04.011

Makovsky, Y., Neuman, A., Surdyaev, A., M., E., 2018. General trends of the top-most sand unit aling the coastline of southern and central Israel.

Mandlier, P.G., Kench, P.S., 2012. Analytical modelling of wave refraction and convergence on coral reef platforms: Implications for island formation and stability. Geomorphology 159–160, 84–92. https://doi.org/10.1016/j.geomorph.2012.03.007

Marrack, E.C., 1999. The Relationship between Water Motion and Living Rhodolith Beds in the Southwestern Gulf of California, Mexico. Palaios 14, 159. https://doi.org/10.2307/3515371

Mauz, B., Hijma, M.P., Amorosi, A., Porat, N., Galili, E., Bloemendal, J., 2013. Aeolian beach ridges and their significance for climate and sea level: Concept and insight from the Levant coast (East Mediterranean). Earth-Science Rev. 121, 31–54. https://doi.org/10.1016/j.earscirev.2013.03.003

Miramontes, E., Thiéblemont, A., Babonneau, N., Penven, P., Raisson, F., Droz, L., Jorry, S.J., Fierens, R., Counts, J.W., Wilckens, H., Cattaneo, A., Jouet, G., 2021. Contourite and mixed turbidite-contourite systems in the Mozambique Channel (SW Indian Ocean): Link between geometry, sediment characteristics and modelled bottom currents. Mar. Geol. 437, 106502. https://doi.org/10.1016/j.margeo.2021.106502

Mitchell, B.G., Bricaud, A., Carder, K., Cleveland, J., Ferrari, G., Gould, R., Kahru, M., Kishino, M., Maske, H., Moisan, T., Moore, L., Nelson, N., Phinney, D., Reynolds, R., Sosik, H., Stramski, D., Tassan, S., Trees, C., Weidemann, A., Vodacek, A., 2000. Determination of spectral absorption coefficients of particles, dissolved material and phytoplankton for discrete water samples. NASA Tech. Memo. 125–153.

Nagasawa, M., Niwa, Y., Hibiya, T., 2000. Spatial and temporal distribution of the wind-induced internal wave energy available for deep water mixing in the North Pacific. J. Geophys. Res. Ocean. 105, 13933–13943. https://doi.org/10.1029/2000JC900019

Neev, D., Bakler, N., Emery, K.O., 1987. Mediterranean coasts of Israel and Sinai: Holocene Tectonism from Geology, Geophysics, and Archaelogy. Taylor & Francis, New York. https://doi.org/10.1016/0025-3227(88)90134-X

Nielsen, T., Knutz, P.C., Kuijpers, A., 2008. Seismic Expression of Contourite Depositional Systems, in: Rebesco, M., Camerlenghi, A. (Eds.), Contourites. Springer, Developments in Sedimentology 60, pp. 301–321. https://doi.org/10.1016/S0070-4571(08)10016-4

Oba, R., Finette, S., 2002. Acoustic propagation through anisotropic internal wave fields: Transmission loss, cross-range coherence, and horizontal refraction. J. Acoust. Soc. Am. 111, 769–784.

https://doi.org/10.1121/1.1434943

Olbers, D., Eden, C., 2016. Revisiting the Generation of Internal Waves by Resonant Interaction with Surface Waves. J. Phys. Oceanogr. 46, 2335–2350. https://doi.org/10.1175/JPO-D-15-0064.1

Ozer, T., Gertman, I., Kress, N., Silverman, J., Herut, B., 2017. Interannual thermohaline (1979–2014) and nutrient (2002–2014) dynamics in the Levantine surface and intermediate water masses, southeastern Mediterranean Sea. Glob. Planet. Change 151, 60–67. https://doi.org/10.1016/j.gloplacha.2016.04.001

Paulat, M., Lüdmann, T., Betzler, C., Eberli, G.P., 2019. Neogene palaeoceanographic changes recorded in a carbonate contourite drift (Santaren Channel, Bahamas). Sedimentology 66, 1361–1385. https://doi.org/10.1111/sed.12573

Peleg, O., Guy-Haim, T., Yeruham, E., Silverman, J., Rilov, G., 2020. Tropicalisation may invert trophic state and carbon budget of shallow temperate rocky reefs. J. Ecol. 108, 844–854. https://doi.org/10.1111/1365-2745.13329

Polton, J.A., Smith, J.A., MacKinnon, J.A., Tejada-Martínez, A.E., 2008. Rapid generation of high-frequency internal waves beneath a wind and wave forced oceanic surface mixed layer. Geophys. Res. Lett. 35, L13602. https://doi.org/10.1029/2008GL033856

Pomar, L., Baceta, J.I., Hallock, P., Mateu-Vicens, G., Basso, D., 2017. Reef building and carbonate production modes in the west-central Tethys during the Cenozoic. Mar. Pet. Geol. 83, 261–304. https://doi.org/10.1016/j.marpetgeo.2017.03.015

Pomar, L., Morsilli, M., Hallock, P., Bádenas, B., 2012. Internal waves, an under-explored source of turbulence events in the sedimentary record. Earth-Science Rev. 111, 56–81. https://doi.org/10.1016/j.earscirev.2011.12.005

Porat, N., Wintle, A.G., Ritte, M., 2003. Mode and timing of kurkar and hamra formation, central coastal plain, Israel. Isr. J. Earth Sci. 53, 13–25.

Quaresma, L.S., Vitorino, J., Oliveira, A., da Silva, J., 2007. Evidence of sediment resuspension by nonlinear internal waves on the western Portuguese mid-shelf. Mar. Geol. 246, 123–143. https://doi.org/10.1016/j.margeo.2007.04.019

Reich, T., Ben-Ezra, T., Belkin, N., Tsemel, A., Aharonovich, D., Roth-Rosenberg, D., Givati, S., Bialik, O.,

Herut, B., Berman-Frank, I., Frada, M., Krom, M.D., Lehahn, Y., Rahav, E., Daniel Sher, 2021. Seasonal dynamics of phytoplankton and bacterioplankton at the ultra-oligotrophic southeastern Mediterranean Sea. bioRxiv. https://doi.org/10.1101/2021.03.24.436734

Reiche, S., Hübscher, C., Brenner, S., Betzler, C., Hall, J.K., 2018. The role of internal waves in the late Quaternary evolution of the Israeli continental slope. Mar. Geol. 406, 177–192. https://doi.org/10.1016/j.margeo.2018.09.013

Rilov, G., 2016. Multi-species collapses at the warm edge of a warming sea. Sci. Rep. 6, 36897. https://doi.org/10.1038/srep36897

Rilov, G., 2013. Regional extinctions and invaders' domination: an ecosystem phase-shift of Levant reef. Rapp. la Comm. Int. pour l'Exploration Sci. la Mér Méditerranée, 40, 782–783.

Rilov, G., Galil, B., 2009. Marine Bioinvasions in the Mediterranean Sea – History, Distribution and Ecology, in: Rilov, G., Crooks, J.A. (Eds.), Biological Invasions in Marine Ecosystems. Springer,Ecological Studies (Analysis and Synthesis) 204, Berlin, Heidelberg, pp. 549–575. https://doi.org/10.1007/978-3-540-79236-9_31

Rilov, G., Peleg, O., Yeruham, E., Garval, T., Vichik, A., Raveh, O., 2018. Alien turf: Overfishing, overgrazing and invader domination in southeastern Levant reef ecosystems. Aquat. Conserv. Mar. Freshw. Ecosyst. 28, 351–369. https://doi.org/10.1002/aqc.2862

Rocha, L.A., Pinheiro, H.T., Shepherd, B., Papastamatiou, Y.P., Luiz, O.J., Pyle, R.L., Bongaerts, P., 2018. Mesophotic coral ecosystems are threatened and ecologically distinct from shallow water reefs. Science (80-.). 361, 281–284. https://doi.org/10.1126/science.aaq1614

Schattner, U., 2021. Isolating the role of shore-parallel sediment transport in continental shelf build-up. Cont. Shelf Res. 225, 104480. https://doi.org/10.1016/j.csr.2021.104480

Schattner, U., Gurevich, M., Kanari, M., Lazar, M., 2015. Levant jet system—effect of post LGM seafloor currents on Nile sediment transport in the eastern Mediterranean. Sediment. Geol. 329, 28–39. https://doi.org/10.1016/j.sedgeo.2015.09.007

Schlager, W., 2005. Carbonate Sedimentology and Sequence Stratigraphy. SEPM concepts in sedimentology and paleontology, volume 8, Tulsa, Oklahoma. https://doi.org/10.2110/csp.05.08

Schmidt, G.M., Wall, M., Taylor, M., Jantzen, C., Richter, C., 2016. Large-amplitude internal waves

sustain coral health during thermal stress. Coral Reefs 35, 869–881. https://doi.org/10.1007/s00338-016-1450-z

Sherman, C., Schmidt, W., Appeldoorn, R., Hutchinson, Y., Ruiz, H., Nemeth, M., Bejarano, I., Motta, J.J.C., Xu, H., 2016. Sediment dynamics and their potential influence on insular-slope mesophotic coral ecosystems. Cont. Shelf Res. 129, 1–9. https://doi.org/10.1016/j.csr.2016.09.012

Sherman, C.E., Locker, S.D., Webster, J.M., Weinstein, D.K., 2019. Geology and Geomorphology, in: Loya, Y., Puglise, K., Bridge, T. (Eds.), Mesophotic Coral Ecosystems. Springer, Coral Reefs of the World 12., pp. 849–878. https://doi.org/10.1007/978-3-319-92735-0_44

Shtienberg, G., Dix, J.K., Roskin, J., Waldmann, N., Bookman, R., Bialik, O.M., Porat, N., Taha, N., Sivan, D., 2017. New perspectives on coastal landscape reconstruction during the Late Quaternary: A test case from central Israel. Palaeogeogr. Palaeoclimatol. Palaeoecol. 468. https://doi.org/10.1016/j.palaeo.2016.12.045

Silva, M., MacDonald, I., 2017. Habitat suitability modeling for mesophotic coral in the northeastern Gulf of Mexico. Mar. Ecol. Prog. Ser. 583, 121–136. https://doi.org/10.3354/meps12336

Sisma-Ventura, G., Yam, R., Kress, N., Shemesh, A., 2016. Water column distribution of stable isotopes and carbonate properties in the South-eastern Levantine basin (Eastern Mediterranean): Vertical and temporal change. J. Mar. Syst. 158, 13–25. https://doi.org/10.1016/j.jmarsys.2016.01.012

Sisma-Ventura, G., Yam, R., Shemesh, A., 2014. Recent unprecedented warming and oligothrophy of the Eastern Mediterranean Sea within the last millennium. Geophys. Res. Lett. 41, 5158–5166. https://doi.org/10.1002/2014GL060393

Smith, T.B., Brandtneris, V.W., Canals, M., Brandt, M.E., Martens, J., Brewer, R.S., Kadison, E., Kammann, M., Keller, J., Holstein, D.M., 2016. Potential Structuring Forces on a Shelf Edge Upper Mesophotic Coral Ecosystem in the US Virgin Islands. Front. Mar. Sci. 3. https://doi.org/10.3389/fmars.2016.00115

Stastna, M., Lamb, K.G., 2008. Sediment resuspension mechanisms associated with internal waves in coastal waters. J. Geophys. Res. 113, C10016. https://doi.org/10.1029/2007JC004711

Storlazzi, C.., Ogston, A.., Bothner, M.., Field, M.., Presto, M.., 2004. Wave- and tidally-driven flow and sediment flux across a fringing coral reef: Southern Molokai, Hawaii. Cont. Shelf Res. 24, 1397–

1419. https://doi.org/10.1016/j.csr.2004.02.010

Studivan, M.S., Voss, J.D., 2018. Population connectivity among shallow and mesophotic Montastraea cavernosa corals in the Gulf of Mexico identifies potential for refugia. Coral Reefs 37, 1183–1196. https://doi.org/10.1007/s00338-018-1733-7

Talley, L.D., Pickard, G.L., Emery, W.J., Swift, J.H., 2011. Descriptive Physical Oceanography: An Introduction, 6th ed. Elsevier - Academic Press, Amsterdam.

Thingstad, T.F., Krom, M.D., Mantoura, R.F.C., Flaten, G.A.F., Groom, S., Herut, B., Kress, N., Law, C.S., Pasternak, A., Pitta, P., Psarra, S., Rassoulzadegan, F., Tanaka, T., Tselepides, A., Wassmann, P., Woodward, E.M.S., Riser, C.W., Zodiatis, G., Zohary, T., 2005. Nature of Phosphorus Limitation in the Ultraoligotrophic Eastern Mediterranean. Science (80-.). 309, 1068–1071. https://doi.org/10.1126/science.1112632

Valle-Levinson, A., Kourafalou, V.H., Smith, R.H., Androulidakis, Y., 2020. Flow structures over mesophotic coral ecosystems in the eastern Gulf of Mexico. Cont. Shelf Res. 207, 104219. https://doi.org/10.1016/j.csr.2020.104219

van Haren, H., 2017. Internal Waves and Bedforms, in: Guillén, J., Acosta, J., Chiocci, F., Palanques, A. (Eds.), Atlas of Bedforms in the Western Mediterranean. Springer International Publishing, Cham, pp. 25–28. https://doi.org/10.1007/978-3-319-33940-5_5

Wang, Y.-H., Dai, C.-F., Chen, Y.-Y., 2007. Physical and ecological processes of internal waves on an isolated reef ecosystem in the South China Sea. Geophys. Res. Lett. 34, L18609. https://doi.org/10.1029/2007GL030658

Williams, D.M., Wolanski, E., Andrews, J.C., 1984. Transport mechanisms and the potential movement of planktonic larvae in the central region of the Great Barrier Reef. Coral Reefs 3, 229–236. https://doi.org/10.1007/BF00288259

Wolanski, E., Delesalle, B., 1995. Upwelling by internal waves, Tahiti, French Polynesia. Cont. Shelf Res. 15, 357–368. https://doi.org/10.1016/0278-4343(93)E0004-R

Woodson, C.B., 2018. The fate and impact of internal waves in nearshore ecosystems. Ann. Rev. Mar. Sci. 10, 421–441. https://doi.org/10.1146/annurev-marine-121916-063619

Wyatt, A.S.J., Leichter, J.J., Toth, L.T., Miyajima, T., Aronson, R.B., Nagata, T., 2020. Heat accumulation

on coral reefs mitigated by internal waves. Nat. Geosci. 13, 28–34. https://doi.org/10.1038/s41561-019-0486-4